Analytical Methods

Accepted Manuscript

This article can be cited before page numbers have been issued, to do this please use: A. Parmar, A. Kanjirakat, V. Fernandes and N. K. Mani, *Anal. Methods*, 2026, DOI: 10.1039/D6AY00583G.

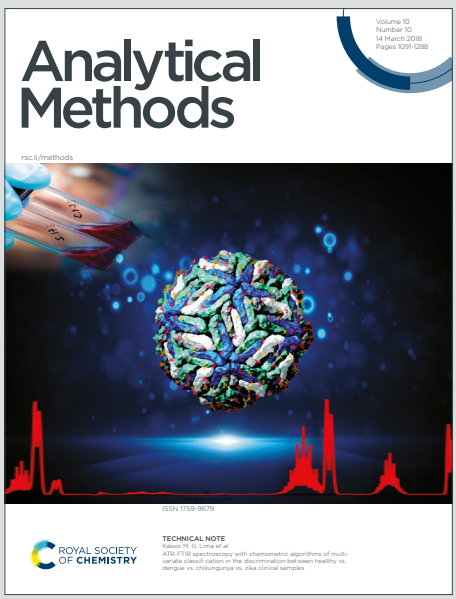

View Article Online
DOI: 10.1039/D6AY00583G

ARTICLE

A Novel Bubble Rupture Sensing Methodology for Sweat-Driven Disease Diagnostics

Received 00th January 20xx,
Accepted 00th January 20xx

DOI: 10.1039/x0xx00000x

Akshay Ajit Parmar[a±], Anoop Kanjirakat[a±], Dolfred Vijay Fernandes[a], Naresh Kumar Mani[a*]

Sweat is a rich biofluid whose composition depends heavily on physiology and varies systematically across a range of systemic and dermatological conditions, making it an attractive medium for non-invasive diagnostics. However, existing diagnostic tools, which rely primarily on electrochemical ion-selective electrodes and optical microfluidic systems, require complex instrumentation and have significant limitations in ease of application and deployment. This poses a need for a low-cost, simple sensing approach using sweat as a sample for disease detection. Here we demonstrate a novel bubble sensing methodology that exploits the relationship between bubble film stability and electrolyte concentration in a reagent-free setup requiring no electrochemical transduction. A controlled-volume bubble was made using a sodium dodecyl sulphate–glycerol solution, which was then tested by adding potassium chloride (KCl) solutions at concentrations of 0.01–0.15 mol L^{-1}, simulating sweat at variable ionic strengths. Two characteristic timescales were identified: the time to burst (t_b), measured by the naked eye on a seconds timescale, and the film retraction time (τ), resolved at 100,000 frames per second using a high-speed camera. The time to burst exhibited a strong exponential decay with increasing KCl concentration (R^2 = 0.934), with greatest sensitivity in the healthy resting sweat range (0.01–0.1 mol L^{-1}) and a plateau at pathological concentrations above 0.1 mol L^{-1}. High-speed imaging revealed distinct changes in rupture initiation location and film retraction behaviour upon analyte addition, with retraction time increasing from 250 µs in control bubbles to ~1.5 ms. The observed trend was quantitatively reproduced using a coupled DLVO-Kramers nucleation model, identifying electrostatic double-layer screening as the primary mechanism driving faster rupture at higher ionic strength. This work establishes the proof of concept for bubble rupture dynamics as a functional sensing mechanism and provides the basis for further development of surfactant bubble-based biosensors.

.

Keywords: Bubble rupture, Non-invasive diagnosis, Ionic strength, Label-free, Sweat.

1. Introduction

Disease progression is generally detected using invasive and non-invasive body fluids. Among non-invasive fluids sweat has emerged as a reliable diagnostic biofluid owing to its non-invasive accessibility and rich biochemical signature [1,2,3]. Unlike blood, which remains the clinical gold standard for diagnostics, but requires invasive puncture and trained personnel. Sweat on the other hand can be sampled continuously and non-invasively from the skin, making it ideal for point-of-care and wearable applications [4,5]. Beyond its collection convenience, sweat contains a wide range of biomarkers electrolytes, metabolites, hormones, and proteins, whose concentrations reflect underlying systemic physiology [6]. These properties have driven the development of flexible wearable sensors for real-time sweat analysis, used in health monitoring, exercise, drug metabolism, and ethanol detection. [4,5,7].

The biochemical composition of eccrine sweat is derived primarily from the ultrafiltration of blood plasma, with active electrolyte reabsorption and secretion occurring as the fluid moves along the sweat duct [6,8]. Sodium and chloride are the dominant ionic species, typically present at concentrations of 10-80 mM, while potassium occurs at lower levels of 2-10 mM; additional constituents include glucose, lactate, urea, ammonia, bicarbonate, and various micronutrients [6,8]. Because eccrine glands selectively reabsorb electrolytes, discharged sweat is hypotonic relative to plasma, and the precise ionic composition varies with sweat rate, body region, and individual metabolic state [8]. While the transport mechanisms governing sodium and chloride are well characterised, those of many other sweat constituents remain incompletely understood, and direct correlations between sweat and blood concentrations are not firmly established for most analytes [6]. This homeostatic regulation is disrupted across a range of pathological conditions, producing disease conditions and quantifiable changes in sweat electrolyte composition. In Cystic Fibrosis (CF), mutations in the CFTR gene impair ductal chloride reabsorption, elevating sweat chloride to ≥60 mmol/L, a threshold that is clinically diagnostic for the condition, compared to normal values below 29 mmol/L [9,10].

In Chronic Kidney Disease a reduction in renal clearance drives compensatory excretion of nitrogenous waste products and electrolytes, including potassium and urea through the sweat glands, altering ionic strength and metabolite composition [11,12]. Diabetic autonomic neuropathy disrupts neural regulation of eccrine gland

[a] *Manipal Institute of Technology, Manipal Academy of Higher Education, Manipal, India. ± Contributed Equally.*
[b] ***Corresponding author:*** *Email: naresh.mani@manipal.edu, maninaresh@gmail.com*

functioning, resulting in elevated sweat sodium and modified osmotic properties [13]. Dermatological conditions such as Atopic Dermatitis and Psoriasis compromise epidermal barrier integrity, increasing trans-epidermal water loss and promoting localised salt accumulation at the skin surface, further elevating ionic concentrations beyond normal conditions [14,15]. Taken together, these associations highlight sweat ionic strength as a sensitive and accessible non-invasive indicator of a broad spectrum of systemic disorders.

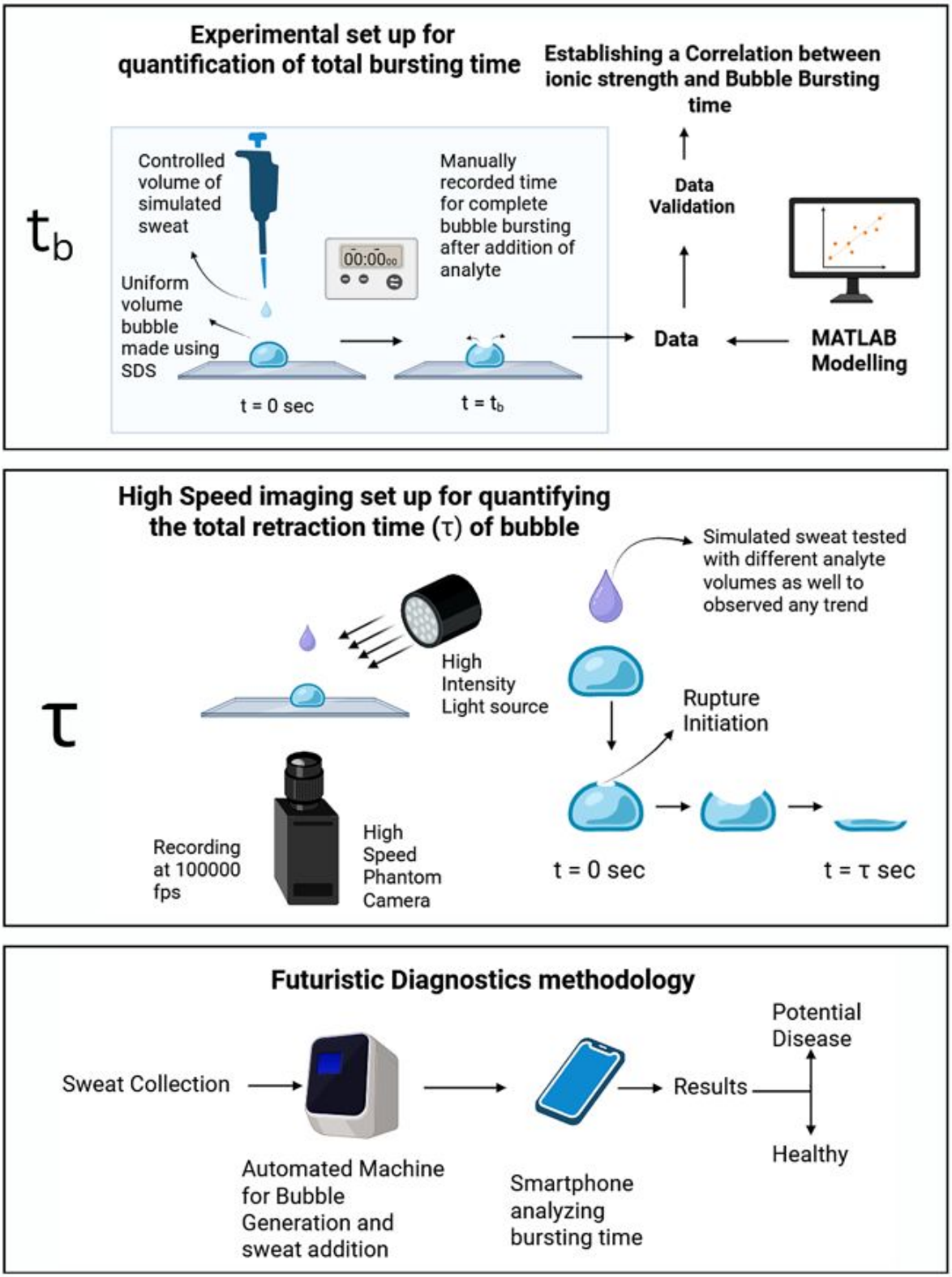

Fig.1 Schematic representation of experimental setup and analysis pipeline for measuring bubble burst time (t_b) and film retraction time (τ).

Electrochemical sensing has dominated efforts to monitor sweat electrolyte composition, with potentiometric ion-selective electrodes (ISEs) representing the most widely adopted sensing mechanism [4,5,7]. ISEs exploit the Nernstian relationship between membrane potential and ionic activity to enable selective detection of Na^+, K^+, Cl^-, Ca^{2+}, and NH_4^+, and have been successfully integrated into flexible wearable patch formats for continuous sweat monitoring [4,5]. Despite their analytical performance, these systems carry practical limitations that constrain their broader deployment. ISE-based platforms require stable reference electrodes, whose miniaturisation and design in wearable formats remains technically challenging and is susceptible to drift and biofouling that necessitate frequent calibration [7]. Amperometric and voltammetric sensors used for metabolite detection require additional requirements for supporting electronics, signal conditioning, and wireless transmission modules, increasing system complexity, cost and feasibility [4,5]. Optical colorimetric microfluidic platforms have been explored as simpler alternatives but typically rely on smartphone-based image analysis or embedded optical elements [16]. Hence, there remains a clear need for a robust, low-cost sensing mechanisms that can respond to changes in ionic composition without relying on complex electrochemical or optical principles.

A novel and largely unexplored sensing modality is offered by bubble-based systems, which exploit the dependence of thin liquid film stability on the physicochemical properties of the surrounding solution. When a bubble forms at a liquid surface, a free-standing thin film cap is established whose drainage and rupture are governed by surface tension, viscosity, ionic concentration, and interfacial forces [17,18]. Variations in electrolyte concentration modify these interfacial interactions [19], most notably through screening of electrostatic double-layer repulsion, thereby altering film stability and accelerating rupture [20,21]. Once initiated, rupture propagates as a retraction front through the film [22], a process readily captured by high-speed imaging. Because bubble formation and collapse are optically observable and straightforwardly quantifiable, such platforms offer a reagent-free and instrumentation-light route to detecting changes in solution ionic composition [17]. We hypothesise that a measurable, systematic correlation exists between KCl analyte concentration and bubble film rupture dynamics, providing the basis for a simple, low-cost sensing approach.

In this study, we examine the relationship between ionic concentration and bubble film rupture dynamics, aiming to develop a bubble-based sensing method capable of detecting variations in electrolyte concentration relevant to physiological and pathological states. This work established the proof of concept which can allow for the preliminary screening of patients in point of Care settings for disease which show elevated ion concertation in sweat. Specifically, we study the rupture behaviour of soap bubbles upon the introduction of potassium chloride (KCl) solution at different concentrations, with KCl serving as a physiologically relevant proxy for human sweat. Two distinct timescales to define the rupture process were adopted and explored. The first, called the time to burst (t_b), is the interval between adding a KCl droplet onto the bubble surface and the onset of visible rupture, as observed by the naked eye; this timescale is on the order of seconds. The second, referred to as the retraction time (τ), pertains to the duration of the rupture event itself, from its initiation to its complete film retraction and spans over milliseconds, necessitating high-speed camera imaging for accurate measurement. We observe that t_b shows a systematic dependence on KCl concentration, suggesting its potential as a sensing parameter for quantifying electrolyte levels (Figure 1). KCl concentrations ranging from 0.01 to 0.15 mol L^{-1} are tested, covering a range relevant to the ionic content typically found in human sweat [6,8]. To the best of our knowledge, this represents the first application of bubble rupture dynamics to physiologically relevant electrolyte sensing.

2. Methodology

2.1 Solution Preparation

A surfactant-based bubble solution was prepared using Sodium Dodecyl Sulfate (SDS) and glycerol. Stock solutions of 48 mM SDS and 20% v/v glycerol were prepared separately and mixed in a 1:1 ratio to obtain a final experimental solution containing 24 mM SDS and 10% v/v glycerol. The final SDS concentration corresponded to three times the Critical Micelle Concentration (CMC), ensuring interfacial saturation and stable film formation. The glycerol concentration was optimized to increase viscosity and reduce film thinning due to evaporation and reduce rate of film drainage. To model the electrolyte composition of human sweat, potassium chloride (KCl) analyte solutions were prepared at six different molarities ranging from 0.01 M to 0.15 M.

2.2 Bubble Generation and Measurement of Time to Burst (t_b)

A controlled bubble was generated on a clean glass slide using the prepared SDS-glycerol solution. A micropipette adjusted to 30 µL was used solely to define the volume of air dispensed; upon dipping the pipette tip into the bubble solution, no fluid was actively drawn into the tip. Instead, a minimal and consistent amount of bubble solution was passively captured within the tip via capillary action, forming a uniform thin film of solution across the tip opening. The tip was then brought into contact with the glass slide surface, and the air was slowly dispensed, with the pipette functioning as a blower that expelled the defined air volume through the solution film, producing a bubble of controlled and reproducible volume adhered to the glass slide. Following bubble formation, 5 µL of the KCl analyte solution was gently pipetted onto the bubble surface perpendicularly, and a stopwatch was simultaneously started. The time elapsed between analyte addition and visible bubble rupture was manually recorded. This procedure was repeated across all KCl concentrations tested, and a baseline control experiment was additionally performed using a 30 µL bubble without analyte addition to characterize natural rupture dynamics in the absence of ionic perturbation (Supplementary Information S1 -S4).

2.3 High-Speed Imaging of Film Retraction Time (τ)

Thin-film collapse dynamics were recorded using a Phantom ultra-high-speed optical camera equipped with a magnification lens focused on the glass slide. Imaging parameters were set to a resolution of 128 × 128 pixels at a frame rate of 100,000 frames per second, corresponding to a temporal resolution of 10 µs per frame. To compensate for the reduced exposure time due to high shutter speeds, a high-intensity light source was positioned adjacent to the sample to ensure clear visualisation of thin-film boundaries and rupture propagation. Rupture dynamics were subsequently analysed

by counting the number of frames required for complete film retraction and multiplying by the frame interval of 10 µs to calculate the total retraction time. Frame-by-frame analysis additionally enabled identification of distinct post-rupture behaviours, including symmetric hole expansion, asymmetric rupture propagation, and flapping-flag motion of the retreating film.

3. Results

3.1 Correlation between the ionic strength of analyte and bubble bursting time (t_b)

The relationship between KCl concentration and time to burst was investigated across a range of normal and diseased physiological concentrations (0.01–0.15 mol L^{-1}). The data were fitted to an exponential decay function, yielding the equation mentioned in Figure 2, with a coefficient of determination of $R^2 = 0.934$, indicating a strong fit between the model and the experimental data. As shown in the graph, time to burst decreases sharply with increasing KCl concentration at lower concentrations, before plateauing at approximately 3.61 seconds at higher concentrations. This behaviour is characteristic of an exponential decay curve, as the rate of decrease is greatest at low concentrations and progressively diminishes, asymptotically approaching the plateau value.

particularly useful for distinguishing between normal physiological states. Beyond this region (C > 0.1 mol L^{-1}), the curve plateaus and the burst time shows minimal variation, corresponding to elevated ionic concentrations associated with pathological or diseased conditions, such as those observed in cystic fibrosis or other conditions characterised by abnormal sweat electrolyte levels. This graph acts as a standard for the preliminary screening of patients which are diseased (lying outside the blue region) or healthy (inside the blue region). The system therefore functions as a preliminary binary screening tool for distinguishing healthy and pathological ionic ranges.

3.2 High Speed imaging of Bubble Rupture Dynamics

High-speed imaging was performed to visualise and quantify the thin-film retraction dynamics of soap bubbles under control and test conditions. Frame sequences for each experimental condition are presented in Figure 3. For the control bubble (no analyte addition), complete film retraction occurred within 250 µs. The rupture initiated at a single nucleation point and propagated outward symmetrically, with the retraction front expanding radially across the

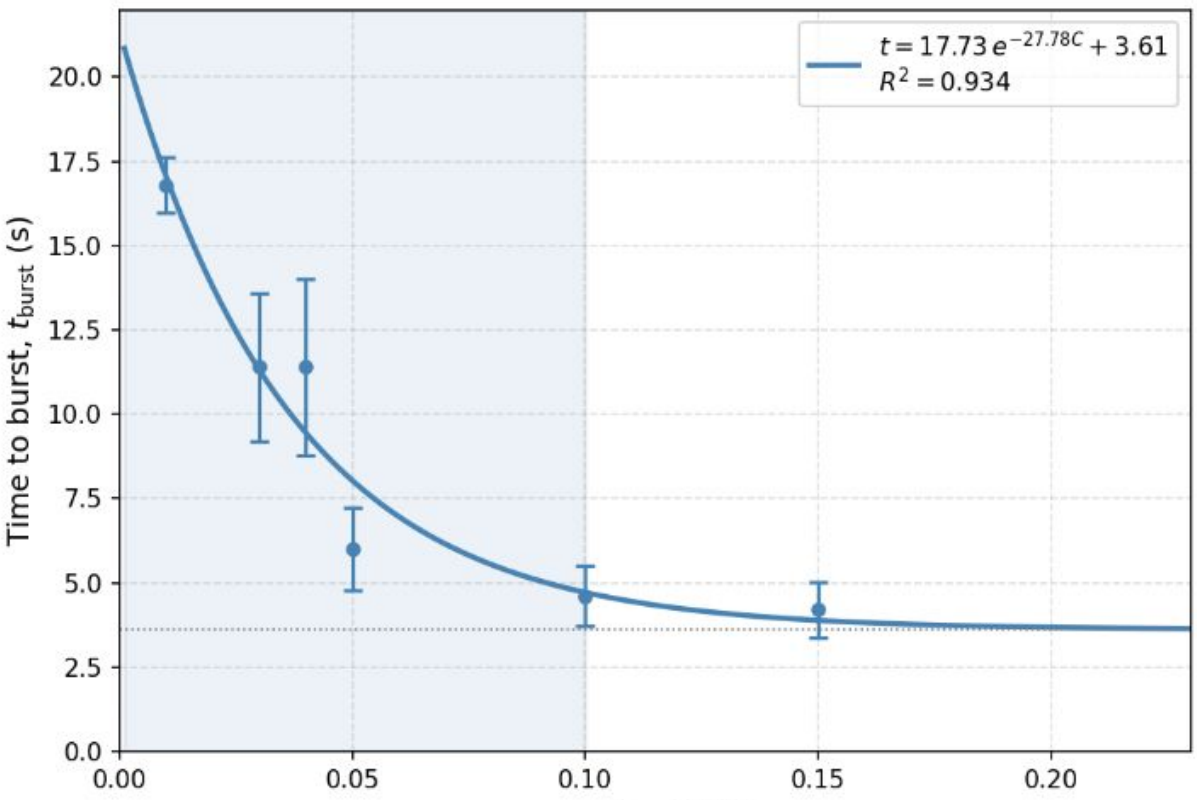

Fig. 2 Trend observed between the ionic strength of analyte and the t_b time.

The lightly shaded blue region in the graph (0.01–0.1 mol L^{-1}) represents the healthy resting sweat ionic strength range, determined from the physiological Na^+ and K^+ ion concentrations present in sweat under normal resting conditions. Within this region, the burst time varies considerably, reflecting the sensitivity of the system to small changes in ionic concentration, a feature that is

bubble cap in a uniform manner consistent with classical hole-opening dynamics. No significant deformation or directional bias was observed in the retracting film. In the test condition at 0.15 M KCl with a 5 µL analyte volume, the total retraction time increased markedly to 1.52 ms. Rupture initiation was observed to occur at variable locations across the bubble surface, and the retraction

proceeded asymmetrically. The film exhibited irregular, non-uniform collapse behaviour, with the rupture front propagating inward rather than outward, reflecting a directional asymmetry absent in the control condition. At the same concentration (0.15 M KCl) with an increased analyte volume of 10 µL, the retraction time was 1.57 ms, comparable to the 5 µL condition, indicating that the additional analyte volume produced negligible further increase in collapse duration. However, a notable qualitative difference in rupture behaviour was observed: rupture consistently initiated at the analyte-bubble interface at the base of the bubble, and the subsequent film retraction exhibited a pronounced torsional twist during collapse. This reproducible asymmetric retraction pattern contrasted with the spatially variable rupture initiation observed at 5 µL. Across all test conditions, the presence of the KCl analyte produced a substantial and consistent increase in retraction time relative to the control, with the primary effect saturating between 5 µL and 10 µL analyte volumes at 0.15 M concentration (Figure 3).

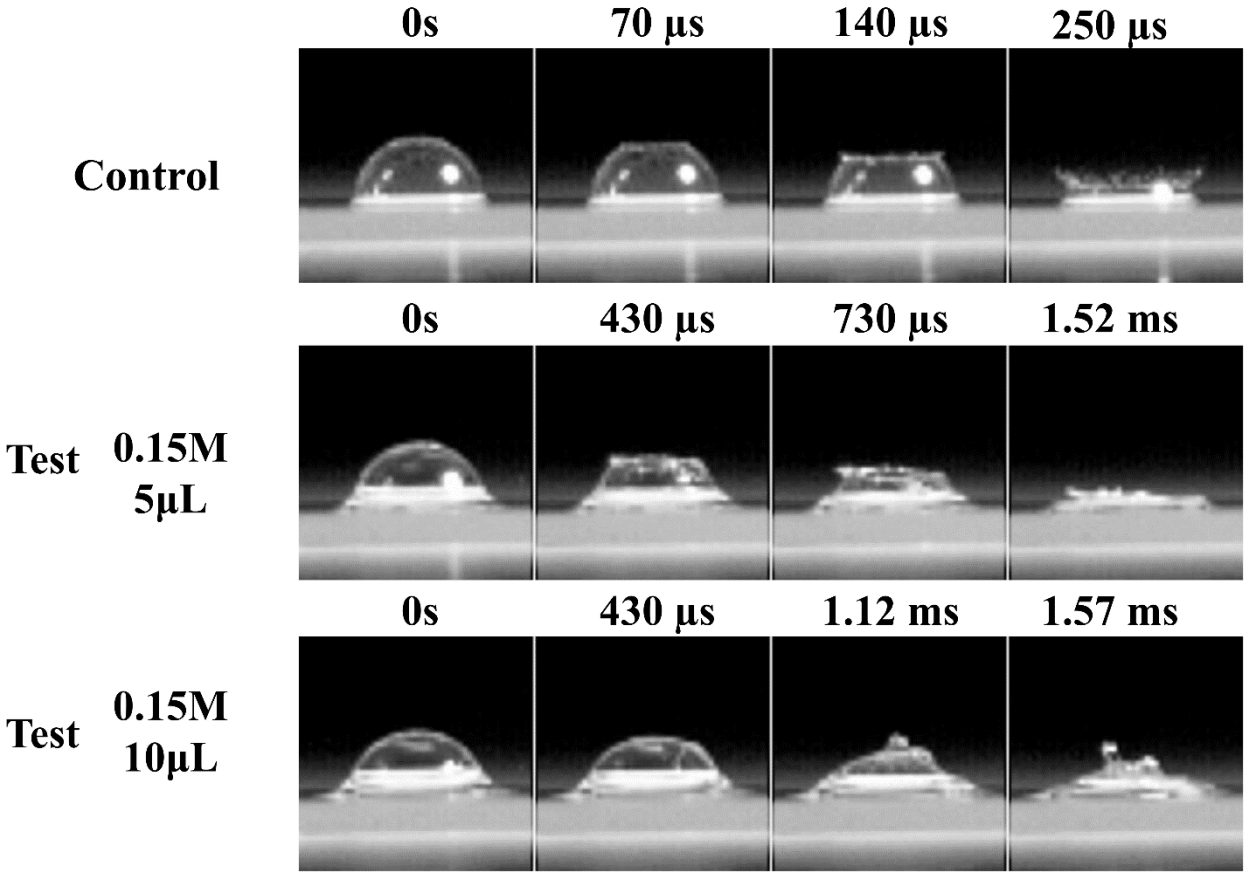

Fig. 3 High-speed camera images of the bubble to capture the retraction time (τ), comparing the time for complete retraction of the control bubble and when an analyte of high ionic concentration is added.

4. Discussion

When a drop of KCl analyte is added to the bubble, several simultaneous physicochemical processes within the thin liquid film of the bubble are initiated. The bubble cap is a free-standing film stabilized by electrostatic repulsion between its two negatively charged air-water interfaces, each coated with adsorbed dodecyl sulphate anions (DS^-) from SDS. Upon introduction of K^+ and Cl^- ions, the diffuse electrical double layers at these interfaces are compressed, and the Debye screening length is shortened [23,24]. This reduces the range and magnitude of inter-surface repulsion, accelerating the viscous drainage of the film [25]. In addition, two other processes are also activated upon KCl addition. First, K^+ ions react with dissolved DS^- to precipitate potassium dodecyl sulphate (KDS), a sparingly soluble salt [26,27]. Although precipitation of KDS could theoretically reduce the free dodecyl sulphate concentration in solution and consequently elevate surface tension, this mechanism is suppressed in the current system, as SDS exceeds the CMC by more than 3-fold. At higher SDS concentrations, the micellar reservoir maintains full interfacial saturation over the entire experimental KCl range, keeping the surface tension fixed at its CMC plateau value [28]. The micellar reservoir continuously replenishes interfacial DS^- coverage, keeping the surface fully saturated and maintaining a steady surface potential. The disturbance to the surface potential is therefore minimal. Similarly, the influence of Marangoni flow along the film surface is also negligible for the same reason. Second, KDS microcrystals precipitating in the bulk may lodge within the Plateau borders, partially impeding film drainage due to Pickering resistance [29]. However, this effect is negligible since the KDS crystal volume fraction is too small to affect drainage viscosity. The system, therefore, constitutes a well-controlled, single-mechanism experiment in which the reduction in bubble lifetime with increasing KCl concentration is solely due to DLVO electrostatic screening.

To explain the experimentally observed exponential decay in bubble burst time with increasing analyte concentration, a combined mathematical model has been developed. This model comprises the Reynolds lubrication equation, which characterizes the reduction in the cap film thickness over time resulting from the interplay between capillary pressure, which facilitates drainage, and DLVO disjoining

pressure, which opposes it [30]. Additionally, it incorporates Kramers nucleation theory, which estimates the average duration for a thermal fluctuation to cause the rupture of the film upon reaching its equilibrium thickness [31]. The model is governed by a set of universal physical constants and system-specific parameters, all listed in Table 1. The model is solved using an in-house MATLAB code.

The description of thin film drainage of a bubble layer under axisymmetric conditions is given by the Reynolds lubrication partial differential equation for the spatially resolved thickness $h(r, t)$:

$$\frac{\partial h}{\partial t} = \frac{1}{3\mu r}\frac{\partial}{\partial r}\left[rh^3\left(\frac{\partial P_{net}}{\partial r}\right)\right] \quad (1)$$

where r is the radial coordinate, μ is the liquid viscosity and $P_e(r, t) = P_{cap} - \Pi[h(r, t)]$ is the local net thinning pressure, comprising the capillary pressure $P_{cap} = 2\gamma/R$ and the DLVO disjoining pressure Π [31]. The dynamic viscosity is $\mu = 2.5 \times 10^{-3}$ Pa s, corresponding to a ~30% v/v glycerine–water mixture, and the surface tension is $\gamma = 0.065$ N m^{-1}, consistent with an SDS solution at three times the critical micelle concentration where the interface is fully saturated and γ is independent of further surfactant addition [28]. The bubble radius is assumed at $R = 1.5 \times 10^{-3}$ m, giving a constant capillary driving pressure.

Table 1. *Model parameters and physical constants*

Symbol	Value	Units	Description
k_B	1.381×10^{-23}	J K^{-1}	Boltzmann constant
T	298	K	Temperature
e	1.602×10^{-19}	C	Elementary charge
N_A	6.022×10^{23}	mol^{-1}	Avogadro number
ε_0	8.854×10^{-12}	F m^{-1}	Vacuum permittivity
ε_r	80	—	Relative permittivity of water
R	1.5×10^{-3}	m	Bubble radius
A_H	3.7×10^{-21}	J	Hamaker constant (air–water–air)
h_0	1×10^{-6}	m	Initial film thickness
h_c	5×10^{-9}	m	Newton black film reference thickness
n_0	$2N_A c$	m^{-3}	Bulk ion number density
κ	$(2N\_Ae^2c/\varepsilon_0\varepsilon_r k_B T)$ ^1/2	m^{-1}	Debye screening parameter
λ_D	κ^{-1}	m	Debye screening length

A full mathematical solution of this nonlinear parabolic partial differential equation (PDE) (Eq.1) requires spatial discretisation in r, a symmetry condition at the apex, and a plateau border pressure condition at r = R .Since our interest is the scalar burst time rather than the spatially-resolved thinning profile, the partial differential equation is reduced to a tractable lumped ordinary differential equation by assuming the film thickness is spatially uniform at every instant, replacing the radial pressure gradient by its global scale estimate $\partial P_e/\partial r \sim P_e/R$. This yields the governing equation for $h(t)$ [30]:

$$\frac{dh}{dt} = -\frac{h^3}{3\mu R^2}\left(P_{cap} - \Pi(h)\right) \quad (2)$$

The total DLVO disjoining pressure Π(h) is the sum of the electrostatic double-layer (EDL) and van der Waals (vdW) contributions, which can be expressed as

$$\Pi(h) = 64\, n_0 k_B T\, \gamma_{dl}^2\, e^{-\kappa h} - \frac{A_H}{6\pi h^3} \quad (3)$$

where n_0 is the bulk ion number density, k_BT the thermal energy, $\gamma_{dl} = \tanh(e\psi_0 / 4k_BT)$ the dimensionless surface potential parameter, $A_H = 3.7 \times 10^{-21}$ J the Hamaker constant, and κ the Debye screening parameter $\kappa = (2N_Ae^2c / \varepsilon_0\varepsilon_r k_BT)^{1/2}$, whose inverse λ_D (κ^{-1}) sets the range of electrostatic repulsion [32]. The surface potential of the SDS-coated air–water interface is $\psi_0 = -65$ mV, consistent with reported values for SDS films at concentrations above the CMC under low electrolyte conditions [33]. KCl concentration (c) influences the model via κ. Higher KCl concentration compresses the double layer, lowers λ_D, and decreases the EDL pressure. The film drains until it reaches the DLVO equilibrium thickness h_{eu}, defined by $\Pi(h_{eq}) = P_{cap}$. At this point, the net driving force vanishes and drainage ceases.

Figure 4 shows the normalised total DLVO disjoining pressure $\Pi(h)/P_{cap}$ as a function of film thickness h for various KCl concentrations. Here, the dashed horizontal line at unity marks the condition of mechanical equilibrium, $\Pi(h_{eq}) = P_{cap.}$ At higher film thickness (h > 50 nm), all curves converge to zero, reflecting the absence of long-range surface–surface interactions and the film draining freely under capillary pressure alone. As the film thins below approximately 50 nm, the overlapping diffuse EDLs generate a prominent repulsive pressure spike that resists further drainage and stabilises the film. The size and lateral reach of this spike decrease systematically with rising KCl concentration, as the Debye screening length $\lambda_D = \kappa^{-1}$ shortens from about 3.0 nm at 0.01 M to about 0.8 nm at 0.15 M. At very small film thickness (h < 5 nm), all curves pass through a shallow negative minimum where the attractive van der Waals contribution momentarily overcomes the electrostatic repulsion, rendering the film locally unstable and providing the thermodynamic driving force for thermal hole nucleation. The filled circles mark the DLVO equilibrium thickness h_{eu} at each concentration, which decreases monotonically from ~28 nm at 0.01 M to ~8 nm at 0.15 M as the EDL is progressively screened.

Once the film thickness reaches h_{eq}, drainage ceases completely, and there is no viscous flow to drive further thinning. The film is mechanically stable at h_{eq} but thermodynamically metastable. It can only rupture via a thermal fluctuation large enough to nucleate a hole of critical area A_c and overcome the DLVO energy barrier. The energy barrier per unit area required to thin a local patch of film from h_{eq} down to the critical Newton black film thickness h_c = 5 nm [34], against the stabilising disjoining pressure, is:

$$W_{barrier} = \int_{h_c}^{h_{eq}} max\left[\Pi(h) - P_{cap}, 0\right] dh \quad (4)$$

Critically, the area enclosed between each curve and the dashed equilibrium line (shaded area in Fig. 3 for 0.01M KCl) represents the DLVO energy barrier per unit area ($W_{barrier}$). This energy barrier diminishes markedly as salt concentration rises. The mean burst time is then related to this barrier through the Kramers nucleation relation [28]. Here, it is assumed that any system residing in a metastable energy minimum and subjected to stochastic thermal fluctuations will ultimately surmount the energy barrier. The average escape time exhibits an exponential dependence on the barrier height in relation to thermal energy, k_BT [28]:

$$t_{burst} = t_0 \, exp\left(\frac{W_{barrier} \cdot A_c}{k_B T}\right) \quad (5)$$

where A_c is the critical nucleation area, and t_0 is a pre-exponential attempt time. The two free parameters (A_c, t_0) can be fitted to the experimental burst times at 0.01 M and 0.15 M KCl, yielding A_c = 1.00 × 10^{-17} m² and t_0 = 4.02 s.

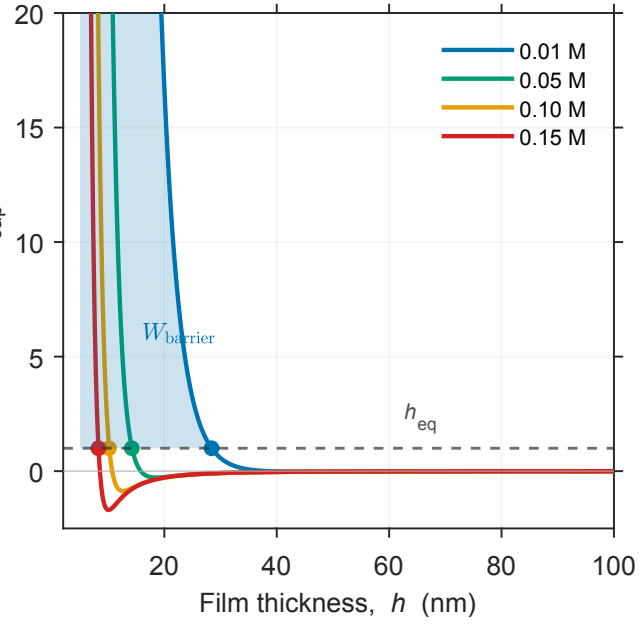

Fig. 4 Normalized total DLVO disjoining pressure to capillary pressure as a function of film thickness for varying KCl concentrations.

Figure 5 presents the model-predicted time to burst (t_{burst}) as a function of KCl concentration. The mathematical model is solved numerically in two sequential steps. First, for each KCl concentration, the DLVO equilibrium thickness is evaluated on a fine discretised grid of 500,000 points spanning $h \in [0.1, 250]$ nm. The Reynolds drainage ordinary differential equation (Eq. 2) is integrated forward in time employing the variable-order stiff solver with relative and absolute tolerances set at 10^{-8} and 10^{-20} meters, respectively. From the numerical analysis, it is observed that the predicted burst time diminishes sharply and nonlinearly as the salt concentration increases, decreasing approximately fourfold across the experimental range before asymptotically approaching a plateau of approximately 4 seconds at high KCl concentrations. This behaviour is a direct consequence of the nature of the pressure variations depicted in Figure 4. The plateau at high concentration arises because once the double layer is fully screened, further addition of KCl produces diminishing returns in barrier reduction as h_{eq} approaches h_c. The concordance between the predicted curve and the experimental data indicates that the DLVO-Kramers framework, with electrolyte concentration incorporated exclusively via the Debye screening parameter κ, is thus deemed adequate to quantitatively represent the concentration dependence of surface bubble lifetime.

High-speed imaging revealed that a flapping-flag-like instability occurred following hole formation once the film thinned to its critical thickness. This behaviour is consistent with the well-characterised aerodynamic coupling mechanism described by Lhuissier and Villermaux [35], in which the retracting rim of a ruptured liquid film undergoes out-of-plane oscillatory motion driven by instability between the rapidly moving film and the surrounding atmosphere. In control bubbles, rupture dynamics proceeded as expected from classical observations [36,37], with symmetric hole expansion and retraction consistent with the Taylor–Culick framework for inviscid liquid films in the absence of compositional heterogeneity [41].

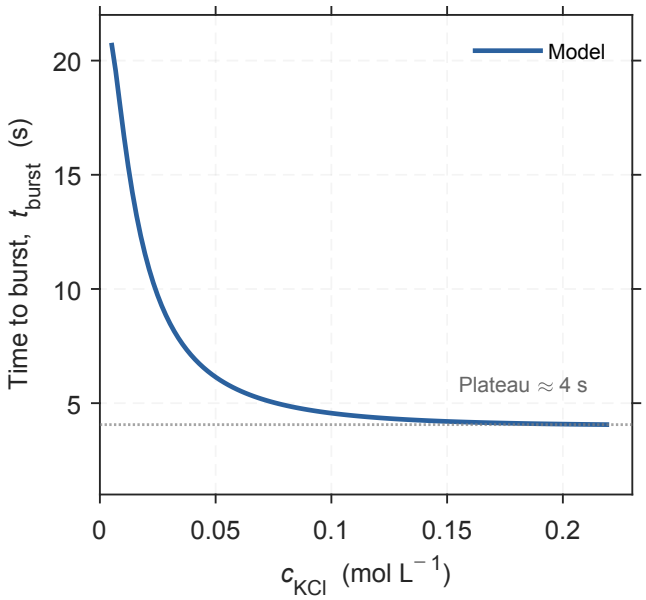

Fig. 5 Model-predicted time to burst as a function of KCl concentration.

In the absence of analyte, bubble rupture occurred predominantly in the outward direction, as expected for symmetric film withdrawal from a point of nucleation. The spatial uniformity of the film composition in this condition yields a uniform surface tension gradient, driving the retraction front radially outward in a manner well described by the classical Taylor-Culick model [36,37,41]. In the presence of the analyte, however, the localised deposition of a KCl-enriched film on the bubble cap produced a spatial pressure gradient that fundamentally altered the directionality of rupture. The inward-directed rupture propagation observed under these conditions indicates a pronounced asymmetry in the stress distribution across the film interface. This behaviour is attributable to the differential thinning induced by the analyte film at the interface, which modifies the local disjoining pressure through screening of the electrostatic double-layer repulsion between the two film surfaces [17,20]. As ionic strength increases, the Debye screening length decreases, compressing the electrical double layer and reducing the repulsive barrier that ordinarily stabilises the film against rupture [17,38]. The consequent localised reduction in film

stability at the analyte contact region creates a stress imbalance that redirects the retraction front inward, toward the bubble interior.

The observed increase in bubble collapse time under the test conditions is interpretable within the Taylor–Culick film retraction model [36,37,41], which expresses the retraction velocity *U* as:

$$U = \frac{dr}{dt} = \sqrt{\frac{2\gamma}{\rho\delta}} \quad (6)$$

where γ represents the surface tension, ρ the liquid density, and δ the film thickness. According to this relationship, the retraction velocity is inversely proportional to the square root of film thickness. High-speed imaging is consistent with the interpretation that the addition of the analyte solution results in the deposition of an additional liquid layer over the bubble cap, effectively increasing the local film thickness. Therefore, the retraction velocity decreases, yielding a longer retraction time (τ) for the bubble film, consistent with the millisecond-scale bursting timescales observed in the experimental conditions. This thickness-velocity coupling is well established in the literature: McEntee and Mysels [39] confirmed the Taylor-Culick prediction experimentally across a range of film thicknesses, and subsequent work by Tammaro et al. [40] extended this analysis to complex non-Newtonian fluids, demonstrating that film rheology and thickness together govern the observed retraction dynamics.

Furthermore, increasing the applied analyte volume from 5 µL to 10 µL produced minimal change in the collapse dynamics. This observation suggests that the saturated film thickness was already reached at approximately 5 µL, and additional liquid did not significantly augment the thickness of the bubble cap. Instead, the excess fluid most likely drained toward the base of the bubble under gravitational and capillary forces [18], rather than contributing to further thickening of the upper film. This behaviour is physically analogous to the drainage dynamics described in thin film hydrodynamics, wherein film thinning and fluid redistribution are governed by the competing effects of capillary pressure, viscous resistance, and body forces [18].At a fixed analyte concentration, the addition of a smaller volume (5 µL) resulted in rupture initiation at variable locations across the bubble surface, exhibiting spatially non-reproducible, asymmetric rupturing. This behaviour is attributed to the partial and spatially heterogeneous disruption of the electrical double layer, arising from non-uniform ionic diffusion and localisation within the film [17,20]. Since a small analyte volume is insufficient to produce a uniformly perturbed interfacial region, the resulting Debye length reduction is spatially variable, producing a randomly distributed array of weakened sites across the film surface [38]. The stochastic nature of rupture initiation under these conditions is consistent with theoretical predictions for films in which the disjoining pressure is heterogeneously modified weak sites nucleate rupture, but their location is governed by the spatial distribution of ionic perturbation rather than a deterministic interfacial geometry [17].

When the analyte volume was increased to 10 µL, rupture consistently initiated at the analyte-bubble interface. Under these conditions, the analyte flowed downward and accumulated at the base of the bubble under gravitational drainage [18], creating a localised region of elevated ionic strength and increasing the probability of precipitate formation at this interface. The accumulation of ions at this locus compresses the electrical double layer to a sufficient degree to locally eliminate the repulsive disjoining pressure [20,38], making the base of the bubble cap the energetically preferred site of rupture nucleation. Rupture from this site produced a reproducible, asymmetric film retraction characterised by a torsional twist in the bubble as it collapsed, a consequence of the off-axis location of the rupture event relative to the bubble's geometric centre, and the resulting asymmetric momentum distribution during film retraction [35,36]. Similar volume-dependent behaviour was observed across higher analyte concentrations, confirming that the delivered analyte volume plays a critical and systematic role in localising rupture initiation and governing post-rupture dynamics. This volume-dependent regime transition from stochastic, multi-site rupture to deterministic, single-site rupture has direct implications for the reproducibility and sensitivity of bubble-based sensing platforms, suggesting that a minimum analyte volume threshold must be satisfied to achieve reliable and spatially reproducible rupture events.

Conclusions

The present work establishes bubble rupture dynamics as a novel and physically grounded transduction mechanism for the detection of electrolyte concentration variations in the physiologically relevant range of 0.01-0.15 mol L^{-1}. To the best of the author's knowledge, this represents the first application of soap bubble thin-film stability as a sensing modality for ionic strength quantification relevant to human sweat diagnostics. Two distinct timescales were identified and characterised as independent sensing parameters. The time to burst (t_b), resolvable by the naked eye on a second's timescale, exhibited a strong exponential decay with increasing KCl concentration (R^2 = 0.934), demonstrating high sensitivity within the healthy resting sweat ionic range and saturation behaviour at concentrations associated with pathological conditions including cystic fibrosis and chronic kidney disease. The film retraction time (τ), resolved at a higher resolution of 10 µs via high-speed imaging at 100,000 frames per second, revealed a transition from rapid symmetric collapse (250 µs) in the absence of analyte to prolonged, asymmetric retraction (~1.5 ms) upon KCl addition, with qualitative rupture behaviour additionally dependent on delivered analyte volume.

The experimental concentration dependence of t_b was quantitatively modelled in MATLAB by a coupled DLVO-Kramer's nucleation framework. The agreement between model predictions and experimental data confirms that compression of the electrostatic double layer is the dominant physicochemical mechanism governing bubble lifetime under the conditions studied, with contributions from Marangoni flow and potassium dodecyl sulphate precipitation shown to be negligible. The platform described here operates without electrochemical transduction, reference electrodes, or reagent consumption, addressing key practical limitations of existing wearable sweat sensing technologies. The t_b parameter is accessible without high-speed instrumentation, offering a low-cost, equipment-light sensing mode suitable for resource-constrained settings. A comparative analysis of existing methods and bubble rupture approach is given in supplementary table 4. This study has been deliberately performed using a homogenous analyte solution of KCl of know solution rather than real sweat to establish a clean and unambiguous correlation between ionic strength and bubble rupture. While sweat contains multivalent ions such as Ca^{2+} and Mg^{2+} they impact the ionic strength by 5% -7% and in this case is assumed to be negligible [6]. However, in such

systems the effect of these parameters still needs to be investigated and can be conducted using a factorial design to understand the contribution of each factor individually while minimising the experiment number.

The parameter t_b can be operationalised in labs and other hospital settings by eliminating the human timing error by adopting a smartphone-based video analysis pipeline. A pixel intensity threshold algorithm would detect the precise movement of the from analyte addition to rupture. Such a model can be developed and tested for accuracy by feeding large datasets for training. This would allow for a more uniform and easy approach for performing the experiment. Alternatively, the entire experiment pipeline for t_b can also be automated using a controlled bubble blower and meter analyte dispersion followed by smartphone recording and result. Future investigations should address validation of the trend using heterogenous slat solution of varying ionic strength and finally observing testing the bubble sensor on real sweat samples. The physical and mechanistic foundations established in this study provide a rigorous basis for such developments and position surfactant bubble rupture as a promising and largely unexplored sensing modality in the broader landscape of non-invasive biofluid diagnostics.

Author contributions

Akshay Ajit Parmar - Writing - Original Draft, Methodology, Validation **Anoop Kanjirakat -** Writing - Original Draft, Methodology, Validation, **Dolfred Vijay Fernandes** - Writing - Original Draft, Writing – Reviewing & Editing, Methodology, **Naresh Kumar Mani** - Writing – review & editing, Validation, Supervision, Project administration, Funding acquisition, Conceptualization.

Conflicts of interest

The authors declare that they have no known competing financial interests or personal relationships that could have appeared to influence the work reported in this paper.

Data availability

All data supporting this study are included within the article and its Supplementary Information. High-resolution figures are provided as TIFF files in the supplementary materials. Bubble bursting video is uploaded along the manuscript files.

Acknowledgements

Authors thank Manipal Institute of Technology, Manipal Academy of Higher Education for their support. This work was carried out at Microfluidics, Sensors & Diagnostics (μSenD) Laboratory, Centre of Microfluidics, Biomarkers, Photoceutics & Sensors (μBioPS), Manipal Academy of Higher Education.

Notes and references

1. Mani NK. Bio-analysis of saliva using paper devices and colorimetric assays. J Anal Test. 2024;8(1):114–132.

2.Mani NK. Tuning hydrophobicity of paper substrates for effective colorimetric detection of glucose and nucleic acids. Anal Bioanal Chem. 2023;415(26):6449–6460.

3.Kelkar N, et al. Sensing of body fluid hormones using paper-based analytical devices. Microchim J. 2022;174:107069.

4.Gu Y, Zhang T, Chen H, Wang F, Pu Y, Gao C, et al. Wearable and flexible electrochemical sensors for sweat analysis: a review. Microsyst Nanoeng. 2023;9:1–19.

5. Jalal NR, Madrakian T, Ahmadi M, Afkhami A, Khalili S, Bahrami M, et al. Wireless wearable potentiometric sensor for simultaneous determination of pH, sodium and potassium in human sweat. Sci Rep. 2024;14:11526.

6. Baker LB. Physiological mechanisms determining eccrine sweat composition. Eur J Appl Physiol. 2020;120(4):719–752.

7. Bandodkar AJ, Jeerapan I, Wang J. Wearable chemical sensors: present challenges and future prospects. Chemosensors. 2023;11(4):244.

8. Baker LB, Wolfe AS. Physiology of sweat gland function: the roles of sweating and sweat composition in human health. Temp (Austin). 2020;7(3):211–259.

9. Schmidt H, Sharma G. Sweat Testing. In: StatPearls [Internet]. Treasure Island (FL): StatPearls Publishing; 2025.

10. Farrell PM, White TB, Ren CL, Hempstead SE, Accurso F, Derichs N, et al. Diagnosis of cystic fibrosis: consensus guidelines from the Cystic Fibrosis Foundation. J Pediatr. 2017;181S:S4–S15.e1.

11. Kovarik JJ, Roetzer-Pejrimovsky T, Schindler M, Pils D, Sunder-Plassmann G, Säemann MD. Decline of kidney function is associated with lower sweat weight in patients with chronic kidney disease. Sci Rep. 2025;15:1–10.

12. Kronfol NO, Lacher DA, Schrier RW. Is there a role for diaphoresis therapy for advanced chronic kidney disease patients? Semin Dial. 2017;30(6):506–513.

13. Verdier-Sévrain S, Bonté F. Skin hydration: a review on its molecular mechanisms. J Cosmet Dermatol. 2007;6(2):75–82.

14. Matthias J, Maul J, Noster R, Meinl H, Chao YY, Gerstenberg H, et al. Sodium chloride is an ionic checkpoint for human TH2 cells and shapes the atopic skin microenvironment. Sci Transl Med. 2019;11:eaau0683.

15. Maifeld A, Wild J, Karlsen TV, Rakova N, Wistorf E, Linz P, et al. Skin sodium accumulates in psoriasis and reflects disease severity. J Invest Dermatol. 2022;142(1):166–178.e8.

16. Nyein HYY, Bariya M, Tran B, Ahn CH, Brown BJ, Ji W, et al. Diving into sweat: advances, challenges, and future directions in wearable sweat sensing. ACS Nano. 2024;18(39):26151–26172.

17. Karakashev SI, Manev ED. Hydrodynamics of thin liquid films: retrospective and perspectives. Adv Colloid Interface Sci. 2015;222:398–412.

18. Karakashev SI, Nguyen AV. Effect of sodium dodecyl sulphate and dodecanol mixtures on foam film drainage: examining influence of surface rheology and intermolecular forces. Colloids Surf A Physicochem Eng Asp. 2007;293(1–3):229–240.

19. Pasquet M, Saint-Anna J, Boulogne F, Rio E. Impact of physical-chemistry on the film thinning in surface bubbles. arXiv:2202.03231. 2022.

20. Jutley MS, Cavalli MR. Stability and nonlinear evolution of electrolyte films: critical thickness and rupture related to Debye screening. Phys Rev E. 2018;98(3):032803.

21. Debrégeas G, de Gennes P-G, Brochard-Wyart F. The life and death of "bare" viscous bubbles. Phys Rev Lett. 2009;103(5):054501.

22. Bico J. Cracks in bursting soap films. J Fluid Mech. 2015;778:1–4.

23. Petkova N, Ivanova-Stancheva D, Grozev NA, Mircheva K, Karakashev SI. Counter-ion effect on the surface potential of foam films and foams stabilized by 0.5 mmol/L sodium dodecyl sulfate. Coatings. 2023;14(1):51.

24. Kontogeorgis GM, Maribo-Mogensen B, Thomsen K. The Debye-Hückel theory and its importance in modeling electrolyte solutions. Fluid Phase Equilibria. 2018;462:130–152.

25. Joye JL, Hirasaki GJ, Miller CA. Dimple formation and behavior during axisymmetrical foam film drainage. Langmuir. 1992;8(12):3083–3092.

26. Hejazi SM, Erfan M, Mortazavi SA. Precipitation reaction of SDS and potassium salts in flocculation of a micronized megestrol acetate suspension. Iran J Pharm Res. 2013;12(3):239.

27. Iranpour T, Mirimba M, Shenouda C, Lynch A, Doucette AA. SDS depletion from intact membrane proteins by KCl precipitation ahead of mass spectrometry analysis. Proteomes. 2025;13(3):30.

28. Rosen MJ, Kunjappu JT. Surfactants and interfacial phenomena. John Wiley & Sons; 2012.

29. Jiang N, Yu X, Sheng Y, Zong R, Li C, Lu S. Role of salts in performance of foam stabilized with sodium dodecyl sulfate. Chem Eng Sci. 2020;216:115474.

30. Wang L. Drainage and rupture of thin foam films in the presence of ionic and non-ionic surfactants. Int J Miner Process. 2012;102:58–68.

31. Langevin D. On the rupture of thin films made from aqueous surfactant solutions. Adv Colloid Interface Sci. 2020;275:102075.

32. Mikhailovskaya A, Chatzigiannakis E, Renggli D, Vermant J, Monteux C. From individual liquid films to macroscopic foam dynamics: a comparison between polymers and a nonionic surfactant. Langmuir. 2022;38(35):10768–10780.

33. Binks BP, Cho W-G, Fletcher PDI. Disjoining pressure isotherms for oil–water–oil emulsion films. Langmuir. 1997;13(26):7180–7185.

34. Evers LJ, Nijman EJ, Frens G. The role of structure in rupturing Newton-black soap films: dynamics of a molecular bilayer. Colloids Surf A. 1999;149(1–3):521–527.

35. Lhuissier H, Villermaux E. Soap films burst like flapping flags. Phys Rev Lett. 2009;103(5):054501.

36. Taylor G. The dynamics of thin sheets of fluid. III. Disintegration of fluid sheets. Proc R Soc Lond A. 1959;253(1274):313–321.

37. Culick FEC. Comments on a ruptured soap film. J Appl Phys. 1960;31(6):1128–1129.

38. Derjaguin BV, Landau L. Theory of the stability of strongly charged lyophobic sols. Acta Physicochim URSS. 1941;14:633–662.

39. McEntee WR, Mysels KJ. The bursting of soap films. I. An experimental study. J Phys Chem. 1969;73(9):3018–3028.

40. Tammaro D, Pasquino R, Villone MM, D'Avino G, Ferraro V, Di Maio E, et al. Bubble rupture and bursting velocity of complex fluids. Langmuir. 2022;38(44):13499–13508.

41. Di Spirito NA, Mirzaagha S, Di Maio E, Grizzuti N, Pasquino R. Bubble rupture and bursting velocity of complex fluids. Langmuir. 2022;38(38):13429–13436.

42. Madhu S, Alam MS, Ramasamy S, Choi J. Wearable, fabric-based microfluidic systems with integrated electrochemical and colorimetric sensing array for multiplex sweat analysis. Chem Eng J. 2025;504:158979.

View Article Online
DOI: 10.1039/D6AY00583G

A Novel Bubble Rupture Sensing Methodology for Sweat-Driven Disease Diagnostics

Akshay Ajit Parmar[a±], Anoop Kanjirakat[a±], Dolfred Vijay Fernandes[a], Naresh Kumar Mani[a*]

Data availability

All data supporting this study are included within the article and its Supplementary Information. High-resolution figures are provided as TIFF files in the supplementary materials. Bubble bursting video is uploaded along the manuscript files.